Article:
Jeannin, M, Bonazzi, T, Gacemi, D et al. (2020) Absorption Engineering in an Ultrasubwavelength Quantum System. Nano Letters, 20 (6). pp. 4430-4436. ISSN: 1530-6984

https://doi.org/10.1021/acs.nanolett.0c01217

Absorption engineering in an ultra-subwavelength quantum system

Mathieu Jeannin,[1] Thomas Bonazzi,[1] Djamal Gacemi,[1] Angela Vasanelli,[1] Lianhe Li,[2] Alexander Giles Davies,[2] Edmund Linfield,[2] Carlo Sirtori[1] and Yanko Todorov[1]*

[1]Laboratoire de Physique de l'Ecole Normale Supérieure, ENS, Paris Sciences et Lettres, CNRS, Université de Paris, 24 Rue Lhomond, 75005 Paris, France

[2]School of Electronic and Electrical Engineering, University of Leeds, Leeds LS2 9JT, United Kingdom

*yanko.todorov@ens.fr

ABSTRACT

Many photonic and plasmonic structures have been proposed to achieve ultra-subwavelength light confinement across the electromagnetic spectrum. Notwithstanding this effort, however, the efficient funneling of external radiation into nano-scale volumes remains problematic. Here we demonstrate a photonic concept that fulfills the seemingly incompatible requirements for both strong electromagnetic confinement and impedance matching to free space. Our architecture consists of antenna-coupled meta-atom resonators that funnel up to 90% of the incident radiation into an ultra-subwavelength semiconductor quantum well absorber of volume $V = \lambda^3 10^{-6}$. A significant fraction of the coupled electromagnetic energy is used to excite the electronic transitions in the quantum well, with photon absorption efficiency 550 times larger than the intrinsic value of the electronic dipole. This system opens important perspectives for ultra-low dark current quantum detectors and for the study of light-matter interaction in the extreme regimes of electronic and photonic confinement.

KEYWORDS: Nanoscale absorbers, metamaterials, optical antennas, strong light-matter coupling.

Achieving strong light absorption is essential for the operation of many optoelectronic devices such as solar cells[1], detectors[2], and saturable absorbers[3]. The recent progress in nano-fabrication techniques has seen the emergence of experiments in which the absorption process is controlled at the single photon, single absorber level[4,5,6]. In bulk materials, light absorption can be simply optimized by increasing the interaction length between the light beam and the material. However, achieving strong absorption in a highly subwavelength structure is a far more difficult task, and is currently an active research topic in the field of nano-optics[7]. This endeavor is particularly pertinent for solid state systems such as quantum wells and dots, as well as for two-dimensional materials[8,9,10]. In all of these systems, the typical de Broglie carrier wavelength is orders of magnitude smaller than the photon wavelength corresponding to the quantum transition of interest. The problem can be illustrated by considering an isolated nanostructure illuminated with intensity I_{in} (Figure 1a), where the efficiency of the absorption process is quantified by the absorption cross section $\sigma_{abs}=P_{abs}/I_{in}$, with P_{abs} the absorbed power. Following Tretyakov,[11] the resonant absorption cross section can be expressed as:

$$\sigma_{abs} = \frac{3\lambda^2}{8\pi\varepsilon}\frac{4\gamma_P\Gamma_{rad}}{\left(\gamma_P+\Gamma_{rad}\right)^2} \quad (1)$$

Here γ_P is the non-radiative loss, Γ_{rad} is the radiation loss (emission rate) of the quantum system, and ε the dielectric constant of the medium surrounding the absorber. The maximum value of σ_{abs} is achieved at the "critical coupling" condition $\gamma_P = \Gamma_{rad}$, but this condition is difficult to satisfy in solid-state systems where the linewidth is dominated by non-radiative decay channels $\gamma_P >> \Gamma_{rad}$.[4] The situation is very severe in the mid-infrared and THz frequency ranges, where the spontaneous emission rate of a single electron is orders of magnitude slower than other

dissipation mechanisms. As illustrated in Figure 1a, in this work we consider a 1x1 μm² absorber that consists of a 32-nm-wide semiconductor quantum well (QW) containing ~10^3 electrons. The first electronic transition of the QW is at f_P = 3.3 THz,[12] corresponding to a wavelength λ = 90 μm that is much larger than the size of the absorber. Eq.1 provides an intrinsic absorption cross section σ_{abs} = 0.047 μm², three orders of magnitude smaller than the theoretical maximum $3\lambda^2/8\varepsilon\pi$= 77 μm², with ε = 12.4. Indeed, the non-radiative rate γ_P = 0.2 THz of the QW is much larger than the radiation loss, Γ_{rad}=3.2x10^{-5} THz (see Supplementary Information for estimations of γ_P and Γ_{rad}).

A solution inspired from microwave technology[13] is to couple the nano-absorber to an antenna that increases the overall radiation loss of the system[14,15]. Such optical antennas can be used to build ultra-fast thermal emitters[16], novel non-linear devices[17,18], and ultra-low dark current infrared detectors[19]. In the optical domain, we can also draw inspiration from the Purcell effect for the emission process[20], which states that the spontaneous emission rate is strongly dependent on the electromagnetic environment. Coupling an emitter to a resonant microcavity can boost or inhibit the spontaneous emission rate[21,22]. In the case of the absorption process, the benefit of microcavities and meta-atom resonators is that they enable electric field confinement into highly subwavelength volumes V_{eff}, comparable with the nano-absorber size[23](Figure 1b). As the light-matter interaction strength scales as $1/V_{eff}^{1/2}$, the absorption rate is increased, and eventually the regime of strong and ultra-strong light-matter coupling can be achieved[12,24,25]. However, a strong electromagnetic confinement suppresses the cavity radiation loss rate, which scales as V_{eff},[26,27] and therefore the microcavity-coupled nano-absorber becomes almost inaccessible to external electromagnetic radiation. In the visible and the near infrared spectral region, several strategies have been proposed to achieve

impedance matching between free space and plasmonic nanostructures.[10,28,29,30]

In this work we demonstrate that is possible to reconcile the antenna concept with the microcavity effect, and to achieve very efficient funneling of incident radiation into a highly subwavelength quantum nano-structure. We introduce a THz photonic arrangement that combines antennas with metamaterial LC (inductor-capacitor)-resonators and concentrates the electric field into nano-volume capacitors filled with semiconductor quantum wells, as illustrated in Figure 1c. In this configuration, the mode of the resonator is matched to free space and (ultra-) strongly coupled with the QW electronic transition.

These concepts, and the following experimental results, have been analyzed in the framework of the temporal coupled mode theory (CMT).[31,32] The CMT provides a set of linear differential equations that describe the temporal evolution of the amplitudes P, a, A of, respectively, the matter oscillator (P), the electric field of the micro resonator (a), and the antenna (A), as a function of the incident wave amplitude (S_{in}). We compare three different cases: matter oscillator P in free space (Figure 1a,d); P coupled with a meta-atom resonator a, which interacts with free space (Figure 1b,e); and, P interacts with an antenna (A)-coupled meta-atom (a) (Figure 1c,f). Each oscillator has its own non-radiative loss rate (γ_P, γ_a, γ_A). By design, the transmission port is absent in our devices, and we consider only the reflection port (S_{out}). As shown in the Supplementary Information, our formalism leads to eq.1 for the case of a single absorber in free space (Figure 1a,d).

As a first step we are interested in understanding how the absorption cross section (eq. 1) is modified in the presence of the resonator, Figure 1b,e and Figure 2. Our resonator is a THz LC

circuit, as described in ref. **12**, where the electric field is compressed into ultra-subwavelength volume, V_{eff}~$10^{-6}\lambda^3$, between the two double-metal capacitive parts of 1 μm² area and thickness 300 nm (Figure 1a). The 300-nm-thin wires of length P_L connecting the capacitors act as inductors and allow the resonant frequency to be tuned in the THz range. The absorbing region, which contains five 32-nm-wide highly doped quantum wells, is placed only in the two capacitive parts (more information in the supplementary material), but owing to surface depletion effects, only the central well is effectively populated at $1.4x10^{11}$ cm^{-2} electrons. The interaction between the QW and the LC resonator is quantified by the coupling strength Ω_R, also known as vacuum Rabi frequency[12]:

$$\Omega_R = \frac{1}{2}\sqrt{\frac{f_{12}e^2(N_1 - N_2)}{m^*\varepsilon\varepsilon_0 V_{eff}}} \quad (2)$$

where f_{12} is the oscillator strength of the transition, e is the electron charge, N_1 and N_2 are the total electron populations in the first and second subbands, respectively, ε_0 is the vacuum permittivity, and m^* is the electron effective mass.

As shown in Figure 2, in order to increase the interaction with the incident light, the antenna-coupled LCs are periodically repeated to form a metamaterial, made up of a unit cell of area Σ such that the beam spot size S of the incident wave covers many unit cells.[11,23] In the metamaterial configuration the ratio between the absorbed and incident power P_{abs}/P_{in} for each unit cell corresponds to σ_{abs}/Σ. In the framework of the CMT, a general expression for the absorption cross section as a function of the power dissipated by the quantum system is:

$$\frac{\sigma_{abs}}{\Sigma} = \frac{2\gamma_p |P|^2}{|S_{in}|^2} =_{def} \eta, \quad (3)$$

Here, $|P|^2$ is proportional to the energy stored in the electronic polarization, and can be related to the density of microscopic dipoles excited by the electric field of the resonator, and $|S_{in}|^2 = \Sigma P_{in}/S$ is the power incident per array unit cell. Eq.3 is a direct consequence of energy conservation and the definition of the absorption cross section[33]. Note that the parameter η quantifies the fraction of photons absorbed by the QW only. The other loss channels, such as the metal losses in the electromagnetic resonators, can also be inferred from CMT, as shown in the Supplementary Information.

The quantity η is not directly provided by experiments, where one instead probes the reflectivity of the system, $R(\omega) = |S_{out}|^2/|S_{in}|^2$. By fitting the experimental reflectivity $R(\omega)$ we can infer the CMT parameters (γ_P, Ω_a, γ_R, Γ_a) and evaluate the absorption cross section from eq.3. The reflectivity spectra $R(\omega)$ were recorded with a dry-air purged Fourier transform infrared spectrometer (FTIR) (Bruker Vertex 70v). We use a proprietary experimental arrangement where a pair of f/1 parabolic mirrors focus the radiation from a Globar source onto the sample and collect the reflected light, which is detected using a He-cooled Ge bolometer (QMC instruments). Light is linearly polarized along the two capacitors of the meta-atoms, and impinges at 45° onto the sample in a transverse magnetic configuration. All spectra are normalized to the reflectivity of a flat Au surface. As a result of the fabrication process, the meta-atoms are placed on the top of 3 μm thick Si_3N_4 layer, which has a flat Au mirror on the bottom that blocks the transmission port[12] (see Supplementary Information for full structure details). Typical reflectivity spectra for a meta-atom (P_L = 11 μm, f_{LC} = 3.2 THz) resonant with the electronic transition are shown in Figure 2b at both room temperature and 7 K. At room temperature, the effect of the electronic absorption is negligible[12], and one observes only the response of the meta-atoms (blue solid line). At 7 K (red solid line), the QW absorption is activated, and the LC mode splits into

lower (LP) and upper (UP) polariton modes, separated by the vacuum Rabi splitting $2\Omega_R$. At low temperature, CMT fits provide typical values $\gamma_a = 0.15$ THz, $\Gamma_a = 0.013$ THz and $\Omega_R = 0.4$ THz. These studies were complemented with data from four other LC structures with $P_L = 9$ μm, 10 μm, 12 μm, and 14 μm (see Supplementary Information). As described in Ref.**12**, these measurements allow the effective volume $V_{eff} = \lambda^3 10^{-6}$ to be obtained from eq.2, which was found to be very close to the geometrical volume of the capacitive parts $V_0 = 0.6$ μm^3, $V_{eff} = 1.2\ V_0$.

The CMT analysis, detailed in the Supplementary Information, shows that the absorbing cross-section σ_{abs} is maximized at the onset of the strong coupling and is expressed as:

$$(4) \qquad \frac{\sigma_{abs}}{\Sigma} = \frac{4\gamma_P \Gamma_a}{\left(\gamma_P + \gamma_a + \Gamma_a\right)^2} \frac{\Omega_R^2}{\Omega_R^2 + \Omega_{R0}^2}$$

This expression is valid for both the weak and strong coupling regime. Here $\Omega_{R0} = \gamma_P/(1+\gamma_P/(\gamma_a + \Gamma_a)) = 0.09$ THz. If the system is in the strong coupling regime, such that $\Omega_R >> \Omega_{R0}$, then eq.4 shows that the peak absorption saturates at a fixed value $\sigma_{abs}/\Sigma = 4\gamma_P\Gamma_a/\left(\gamma_P + \gamma_a + \Gamma_a\right)^2$. This is similar to eq.1, except that now the intrinsic radiation loss of the absorber is replaced with that of the meta-atom resonator, Γ_a.

The corresponding values of $\omega(\eta)$ from eq.3 are plotted in Figure 2c, with peak values η~0.08 at the two polariton states, in agreement with eq. 4. In this case, $\Sigma = 40$ μm², yielding an absorption cross section $\sigma_{abs} = 3.2$ μm². This value is already a significant improvement with respect to the single QW absorber. However, the value η~0.08 and the high reflectivity observed in experiments (Figure 2b) indicate a strong photon rejection rate (85%–90%). Indeed, while the

strong coupling regime is favored because of the dependence $\Omega_R \sim 1/V_{eff}^{1/2}$, the radiative coupling of the resonator vanishes in systems with strong electromagnetic confinement. For instance, in double-metal resonators, the radiation loss is proportional to the thickness of the structure[23]. This is the reason why the radiation loss of the *LC* is very low, $\Gamma_a = 0.013$ THz.

We now demonstrate that this limitation can be lifted in a photonic arrangement based on the strong coupling between antennas with a high radiation loss and the ultra-subwavelength resonators (Figure 3 and Figure 1c,f). As shown in Figure 3a, the antenna element is a large double-metal patch antenna of a total length $L_A = \lambda_A/2n_{eff}$, where λ_A is the resonant wavelength of the antenna and n_{eff} is an effective index. The bulk of the patch antenna is filled with a 3 μm Si_3N_4 layer, which is therefore much thicker than the capacitors of the *LC* structures. The electric field of the fundamental antenna resonances is maximum at the edges, and changes sign in the middle of the antennas[27] (Figure 3a). The symmetry of the antenna resonance thus matches that of the LC mode. Therefore optimal coupling is achieved in the configuration described in Figure 1c and Figure 3a, where each antenna connects the capacitors of two neighboring meta-atoms. Nevertheless, as this system allows a large number of degrees of freedom, many other configurations can be considered, even ones with topologically distinct unit cells. Furthermore, the antennas can be fabricated directly on the bare *LC* resonator arrays, thus allowing a straightforward comparison between uncoupled and antenna-coupled meta-atoms. In Figure 3b, we show reflectivity data for the same *LC* resonator as discussed above ($P_L = 11$μ m) both before (blue solid line), and after (dark green solid line), antenna fabrication. The length of the antenna is $L_A = 5$ μm and it resonates at $f_A = 4.65$ THz; this provides and effective index $n_{eff} \sim 6$. We see that the LC resonance is split into two resonances, A_1 (at 2.67 THz) and A_2 (at 4.8 THz), indicating strong non-perturbative coupling between the antenna and the *LC*. The reflectivity

contrast is strongly improved: 50% as compared to 15% without the antenna. In Figure 3b we also provide electric energy maps obtained by numerical simulations, showing that A_1 is LC-like and A_2 is antenna-like, with A_1 having the same effective volume V_{eff} as the LC alone. CMT fits provide a coupling constant G= –0.6 THz as well as the antenna radiation and non-radiation losses, Γ_A = 0.2 THz and γ_A = 0.85 THz, respectively. We also find that the radiation loss of the antenna-coupled *LC* is strongly$_a$ suppressed, Γ' = 0.0012 THz, so that the interaction with the free-space is essentially mediated by the antenna. The Si_3N_4 layer also introduces a –0.3 THz shift of the *LC* frequency (Supplementary Information).

Next, we examine the performance of such antenna-coupled *LC* structures for enhancing the quantum well absorption. Two types of structures have been studied. The first are the LC structures with variable P_L (9 μm, 10 μm, 11 μm 14 μm), which have been reprocessed with antennas. In this case the antenna resonance is fixed (f_A = 4.65 THz) and the LC resonance is varied, Figure 4a. In the second type of structure, the antenna-coupled LC resonance is designed with a fixed frequency, f_{LC} = 3.35 THz, nearly resonant with the QW absorption (f_P = 3.3 THz). The antenna resonance f_A is then varied by changing the length L_A (5 μm–14 μm), Figure 4b. In Figures 4a,b we show only the low temperature reflectivity spectra (solid lines) where the QW is active; more data is provided in the Supplementary Information. The full system consists of three coupled oscillators, as described in Figure 1c,e, and therefore the reflectivity spectra display three reflectivity minima. All spectra are fitted with the CMT model (dotted lines), which provides almost constant values for G ~ –0.7 THz, resonator loss γ_a = 0.15 THz, Γ_a ~ 10^{-3} THz, as well as the Rabi frequency Ω_R = 0.4 THz. In Figure 4b the loss rates of the antennas evolve monotonically in the range Γ_A = 0.4–0.2 THz and γ_A =0.75–0.45 THz owing to the frequency-dependent loss of the Si_3N_4 layer. All fitting parameters are provided in the Supplementary Information. In Figure 4 the estimations of the photon collection efficiency are provided next to

each experimental spectrum. The peak values have now increased to η~0.2 (Figure 4a) and η ~0.35 (Figure 4b). In Figure 4b it is important to note that as the antenna length L_A increases, the antenna becomes resonant with both the LC and the QW systems, and the area Σ of the array unit cell is increased. As a result, the antenna array with L_A = 12 μm (f_A = 3.3 THz) and Σ= 69 μm² has a maximum absorption cross-section σ_{abs} = 20 μm², which is on the same order of magnitude as the theoretical limit of a single absorber (77 μm²). However, maximum efficiency η~0.35 is obtained for an antenna with L_A = 9 μm (f_A = 3.9 THz), which displayed high radiation loss, Γ_A = 0.3 THz, and a strong reflectivity contrast of 90%.

The analysis based on CMT further uncovers a benefit of the strongly antenna-coupled meta-atoms (Supplementary Information). It shows that the maximum absorption appears at the energy of the electronic transition, and for the case where all three resonators have the same frequency, in accordance with the data from Figure 4. Neglecting the radiation loss from the quantum wells and the meta-atom, the following expression is obtained:

$$\frac{\sigma_{abs}}{\sum} = \frac{\Gamma_A}{\Gamma_A + \gamma_A} \frac{g}{g + \gamma_a} \frac{4(\Omega_R / \Omega_{R1})^2}{\left[1 + (\Omega_R / \Omega_{R1})^2\right]^2} \quad (5)$$

In this formula we have defined $g = G^2/(\Gamma_A+\gamma_A)$ and $\Omega_{R1}^2 = \gamma_P(\gamma_a+g)$. The absorption cross section is thus a bell-like function of the Rabi frequency squared Ω_R^2, and optimal for $\Omega_R\Omega = {}_{R1}$. Using the parameters of our structures, we have g = 0.74 THz and Ω_{R1} = 0.42 THz. Our system with Ω_R = 0.4 THz thus operates very close to the optimal point with maximum possible absorption, $\sigma = \eta_{abs}/ = \Sigma 0.3$. It is interesting to note that in the case where the antenna non-radiative loss γA can be neglected, and a high coupling constant G is achieved, eq.5 predicts

almost unity maximum absorption, regardless of the intrinsic loss γ_P of the absorber. This means that such configuration always allows impedance matching to free space, independent of the physical phenomena that govern γ_P.

In Figure 5, we compare the best results obtained for the photon absorption rate η in our structures with respect to the QW absorber where $\sigma = {}_0\eta_{abs}/(3\lambda^2/8\varepsilon\pi) = 6\text{x}10^{-4}$. The peak value $\eta = 0.33$ for the antenna-coupled LC is 550 times larger than η_0. Furthermore all CMT fits use the same value of the light-matter coupling constant, Ω_R =0.4 THz, meaning that the addition of the antenna layer does not result in a delocalization of the electromagnetic energy and the effective resonator volume remains the same, $V_{eff} = \lambda^3 10^{-6}$. This is confirmed by finite element simulations, which show only a 5% reduction of the *LC* effective volume in the antenna-coupled LC structures. Our system thus reconciles the seemingly incompatible requirements for both strong electromagnetic confinement and impedance matching to free space. Such a photonic architecture can be very beneficial for ultra-low dark current THz quantum detectors, where the electrical area is strongly reduced with respect to the effective absorption cross section of the device.[19,23] In that case, the detector responsivity is proportional to the η coefficient defined in eq. 3, and the ratio between the photocurrent and dark current is provided by the quantity σ_{abs}/s, where *s* the surface of the absorbing region.[19,23] Such devices, which can also operate in the ultra-strong light-matter coupling regime, can also be used to study the effect of the polariton states on the electronic transport.[34, 35] The process that was developed for this demonstration can also be exploited for a large variety of planar antennas coupled with double-metal meta-atoms, and opens many possibilities for the design of perfectly absorbing infrared metamaterials.[36]

ASSOCIATED CONTENT

Supporting Information.

The Supporting Information file contains information about the full layout of the structure, the quantum well absorber, the model based on the coupled-mode theory as well as extended set of additional data.

ACKNOWLEDGMENT

The authors acknowledge the help of the technical staff from the cleanroom facility of Université Paris Diderot, as well help from David Darson (ENS) for the Table of content graphic. This work was supported by the French National Research Agency under the contract ANR-16-CE24-0020, Project Qombs (FET Flagship on Quantum Technologies grant No 820419) and the Engineering and Physical Sciences Research Council (UK) grant EP/P021859/1. EHL acknowledges the support of the Royal Society and Wolfson Foundation.

Notes

The authors declare no competing financial interest.

REFERENCES

1. Nayak, P. K.; Mahesh, S.; Snaith, H. J.; Cahen, D.; Photovoltaic Solar Cell Technologies: Analyzing the State of the Art, *Nat. Rev. Mater.* **2019**, *4*, 269–285.

2. Rosencher E.; Vinter, B.; Optoelectronics **1998**, Cambridge University Press, Cambridge

3. Keller, U. Recent Developments in Compact Ultrafast Lasers. *Nature* **2003**, *424*, 831–838.

4. Gerhardt, I.; Wrigge, G.; Bushev, P.; Zumofen, G.; Agio, M.; Pfab, R.; Sandoghdar, V.; Strong Extinction of a Laser Beam by a Single Molecule, *Phys. Rev. Lett.* **2007** *98*, 033601

5. Rezus, Y.L.; Walt, S.G.; Lettow, R.; Renn, A.; Zumofen, G.; Götzinger, S.; Sandoghdar, V.; Single-Photon Spectroscopy of a Single Molecule, *Phys. Rev. Lett.* **2012** ,*108*, 093601

6. Bharadwaj, P.; Anger, P.; Novotny, L.; Nanoplasmonic Enhancement of Single-Molecule Fluorescence, *Nanotechnology* **2007** *18*, 044017.

7. Schuller, J.A.; Barnard, E.S.;Cai, W.; Jun, Y.C.; White, J.S.; L. Brongersma, M.L.; Plasmonics for Extreme Light Concentration and Manipulation, *Nature Mater.* **2010** *9*,193–204.

8. Parzefall, M.; Szabó, Á.; Taniguchi, T.; Watanabe,K.; Luisier, M.; Novotny L.; Light from Van der Waals Quantum Tunneling Devices, *Nat. Commun.* **2019**, *10*, 1-9

9. Parzefall, M.; Bharadwaj, P.; Jain, A.; Taniguchi, T.; Watanabe, K.; Novotny, L. Antenna-Coupled Photon Emission from Hexagonal Boron Nitride Tunnel Junctions. *Nature Nanotech.* **2015** *10*, 1058–1063.

10. Bisht, A.; Cuadra, J.; Wersäll, M.; Canales, A.; Antosiewicz, T. J.; Shegai, T. Collective Strong Light-Matter Coupling in Hierarchical Microcavity-Plasmon-Exciton Systems. *Nano Lett.* **2019** *19 (1)*, 189– 196.

11. Tretyakov, S.; Maximizing Absorption and Scattering by Dipole Particles *Plasmonics* **2014** *9*, 935-944.

12. Jeannin, M.; Nesurini, G.M.; Suffit, S.; Gacemi, D.; Vasanelli, A.; Li, L.; Davies, A. G.; Linfield, E.; Sirtori, C.; Todorov, Y.; Ultrastrong Light–Matter Coupling in Deeply Subwavelength THz LC Resonators, *ACS Photonics* **2019**, *6*, 1207-1215.

13. Balanis, C.A.; Antenna Theory, **2005** John Wiley & Sons, Hoboken, New Jersey

14. Biagioni, P.; Huang, J. S.; Hecht, B.; Nanoantennas for Visible and Infrared Radiation, *Rep. Prog. Phys.* **2012**, *75*, 024402.

15. Novotny, L.; van Hulst, N. Antennas for Light. *Nature Photon.* **2011** *5*, 83–90.

16. Wojszvzyk, L.; Hector Monin, H.; Jean-Jacques Greffet, J.-J.; Light Emission by a Thermalized Ensemble of Emitters Coupled to a Resonant Structure, *Adv. Opt. Mater.* **2019** *7***,** 1801697, https://doi.org/10.1002/adom.201801697.

17. Fischer, M.P.; Riede, A.; Gallacher, K.; Frigerio, J.; Pellegrini, G.; Ortolani, M.; Paul, D.J.; Isella, G.; Leitenstorfer, A.; Biagioni, P.; Brida. D. Plasmonic Mid-Infrared Third Harmonic Generation in Germanium Nanoantennas. *Light Sci Appl* **2018** *7*, 106.

18. Gigli, C.; Marino, G.; Borne, A.; Lalanne, P; Leo, G.; All-Dielectric Nanoresonators for $\chi(2)$ Nonlinear Optics, *Frontiers in Physics*, **2019**, *7*, 221.

19. Palaferri, D.; Todorov, Y.; Bigioli, A.; Mottaghizadeh, A.; Gacemi, D.;, Calabrese, A.; Vasanelli, A.; Li, L.; Davies, A.G.; Linfield, E.H.; Kapsalidis, F.; Beck, M.;, Faist, J.; Sirtori, C.; Room-Temperature Nine-μm-Wavelength Photodetectors and GHz-Frequency Heterodyne Receivers, *Nature* **2018** ,556, 85−88.

20. Purcell, E. M.; Torrey, H. C.; Pound, R. V.; Resonance Absorption by Nuclear Magnetic Moments in a Solid *Phys. Rev.* **1946** *69*, 37.

21. Gérard, J.M.; Sermage, B.; Gayral,B.; Legrand,B.; Costard, E.; Thierry-Mieg, V.; Enhanced Spontaneous Emission by Quantum Boxes in a Monolithic Optical Microcavity", *Phys. Rev. Lett.* **1998** *81*, 1110.

22. Yablonovitch, E.; Inhibited Spontaneous Emission in Solid-State Physics and Electronics, *Phys. Rev. Lett.* **1987**, *58*, 2059.

23. Palaferri, D.; Todorov, Y.; Mottaghizadeh, A.; Frucci, G.; Biasiol, G.; Sirtori, C.; Ultra-Subwavelength Resonators for High Temperature High Performance Quantum Detectors, *New J. Phys.* **2016,** *18,* 113016.

24. Keller, J.; Scalari, G.; Cibella, S.; Maissen, C.; Appugliese, F.; Giovine, E.; Leoni R.; Beck, M.; Faist, J.; Few-Electron Ultrastrong Light-Matter Coupling at 300 GHz with Nanogap Hybrid LC Microcavities *Nano Lett.* **2017**, *17,* 12, 7410-7415

25. Pelton, M.; Storm, S.D.; Lenga, H.; Strong coupling of emitters to single plasmonic nanoparticles: exciton-induced transparency and Rabi splitting, *Nanoscale*, **2019**, *11*, 14540-14552.

26. Maier, S. A.; Plasmonic Field Enhancement and SERS in the Effective Mode Volume Picture, *Opt. Express* **2006** *14*, 1957.

27. Feuillet-Palma, C.; Todorov, Y.; Steed, R.; Vasanelli, A.; Biasiol, G.; Sorba, L.; Sirtori, C.; Extremely Sub-wavelength THz Metal-Dielectric Wire Microcavities, *Opt. Express,* **2012** *20*, 29121-29130.

28. Li, K.; Stockman, M. I.; Bergman, D.J. Self-Similar Chain of Metal Nanospheres as an Efficient Nanolens, *Phys. Rev. Lett.* **2003**, *91(22)*, 227402

29. Huang, J.-S.; Thorsten Feichtner, T.; Biagioni, P.; Hecht, B.; Impedance Matching and Emission Properties of Nanoantennas in an Optical Nanocircuit, *Nano Lett.* **2009** *9(5)* 1897-1902

30. Spinelli,P.; Hebbink,H.; de Waele, R.; Black,L.; Lenzmann, F.; Polman, A.; Optical Impedance Matching Using Coupled Plasmonic Nanoparticle Arrays, *Nano Lett.* **2011**, *11*, 1760–1765.

31. Haus, H. A.; Waves and Fields in Optoelectronics **2004,** Prentice Hall, Englewood Cliffs, New Jersey (Prentice Hall Series in Solid State Physical Electronics, Holonyak, N.(*Ed*);).

32. Zanotto, S.; Mezzapesa, F.P.; Bianco, F.; Biasiol G.; Baldacci, L.; Vitiello, M.S.; Sorba, L.; Colombelli, R.; Tredicucci, A.; Perfect Energy-Feeding into Strongly Coupled Systems and Interferometric Control of Polariton Absorption, *Nat. Phys.* **2014** *10*, 830–834.

33. Seok, T. J.; Jamshidi, A.; Kim, M.; Dhuey, S.; Lakhani, A.; Choo, H.; Schuck, P. J.; Cabrini, S.; Schwartzberg, A. M.; Bokor, J.; Yablonovitch, E.; Wu, M. C.; Radiation Engineering of Optical Antennas for Maximum Field Enhancement, *Nano Lett.* **2011,** *11*, 2606–2610.

34. Paravicini-Bagliani, G. L.; Appugliese, F.; Richter, E.; Valmorra, F.; Keller, J.; Beck, M.; Bartolo, N.; Rössler, C.; Ihn, T.; Ensslin, K.; Ciuti, C.; Scalari G.; Faist, J.; Magneto-Ttransport Controlled by Landau Polariton States, *Nat. Phys.,* **2018** *15*, 186-190.

35. Naudet-Baulieu, C.; Bartolo,N.; Orso G.; Ciuti C.; Dark Vertical Conductance of Cavity-Embedded Semiconductor Heterostructures, *New J. Phys*. **2019** *21*, 093061.

36. Lee, Y.P., Rhee, J.Y., Yoo, Y.J., Kim, K.W. Metamaterials for Perfect Absorption, **2016** Springer Series in Materials Science, Singapore (Springer Series in Materials Science, *236*, Series Editors: Hull, R., Jagadish, C., Kawazoe, Y., Kruzic, J., Osgood, R.M., Parisi, J., Pohl, U.W., Seong, T.-Y., Uchida, S.-i., Wang, Z.M.).

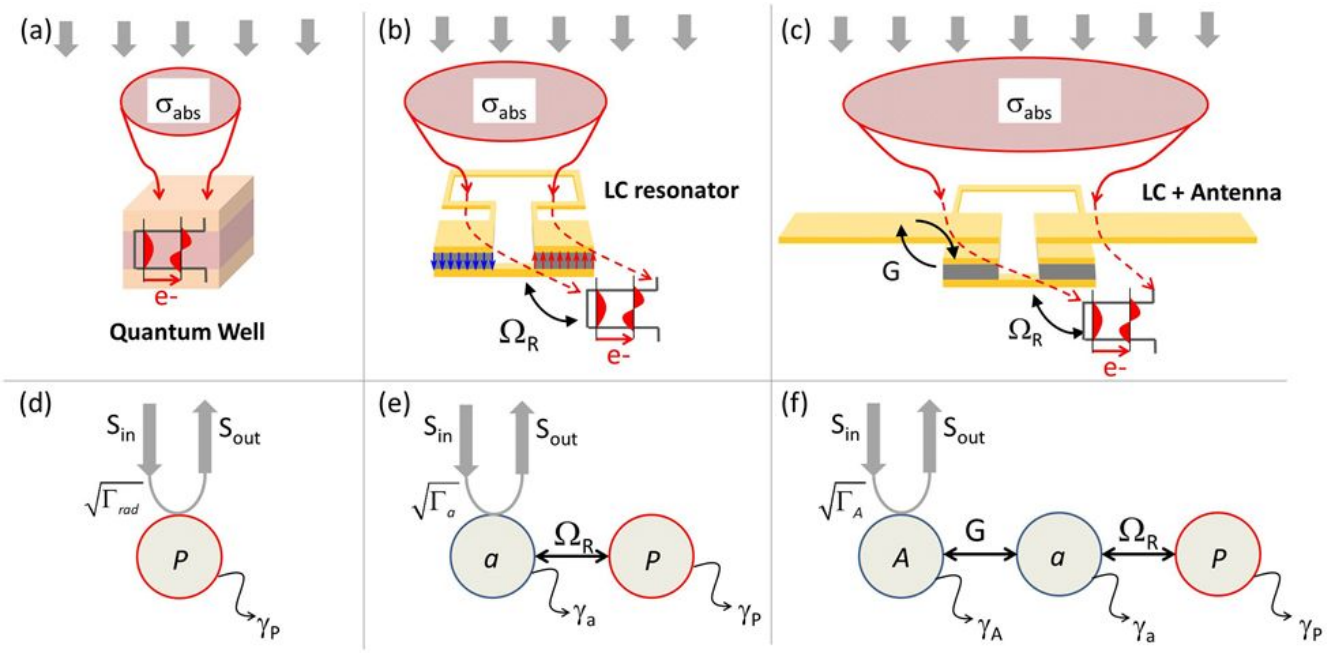

Figure 1. Absorption engineering in a quantum well particle (a) Single nano-absorber (two-level quantum well) interacting with incident infrared radiation. (b) The QW no longer interacts with free space directly, but is coupled to a resonant meta-atom with a coupling rate Ω_R. (c) The coupling to free space is mediated by an additional antenna element interacting with the meta-atom with a coupling rate G. In all cases σ_{abs} denotes the absorption cross-section of the electronic transition only. (d,e,f) Coupled-mode diagrams for the aforementioned cases P: electronic polarization strength, a: electric field amplitude of the LC resonator, A: electric field amplitude of the antenna. S_{in} and S_{out} are the incoming and reflected wave, respectively. The relevant coupling and loss rates are indicated.

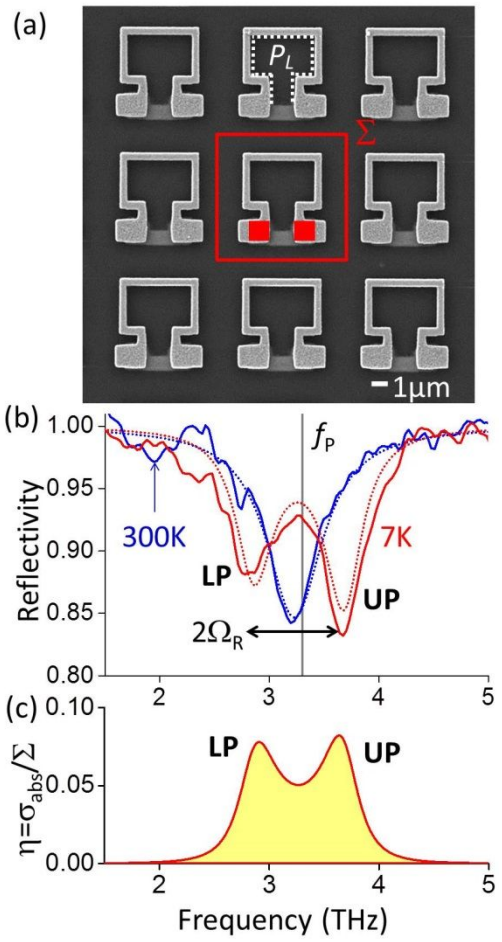

Figure 2. **Quantum well coupled to meta-atom resonator** (a) Electron microscope image of an array of inductor-capacitor (LC) meta-atoms with unit cell Σ where the active region is embedded inside the capacitive elements of the meta-atoms (red squares). P_L denotes the internal perimeter of the inductive loop. (b) Room temperature (blue) and 7 K (red) reflectivity spectra of a structure with P_L =11 μm and f_{LC} = 3.2 THz . Solid lines are experimental data, and dashed lines are obtained using CMT fits. The dotted line shows the electronic transition frequency f_P. LP: lower polariton, UP: upper polariton. The Rabi-splitting extracted from this data is $2\Omega_R = 0.8$ THz. (c) Fraction of photons absorbed η from the CMT fit of panel (b).

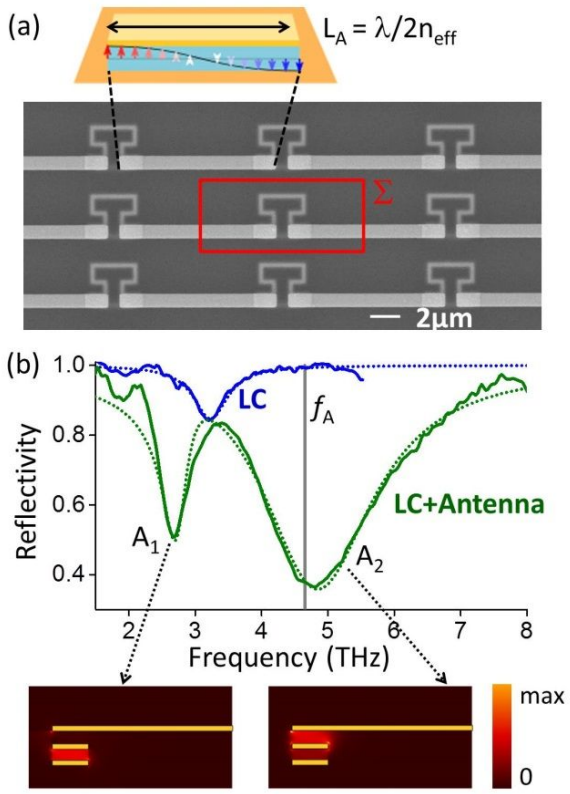

Figure 3. **Antenna-coupled meta-atom** (a) Electron microscope image of the coupled *LC* resonator – antenna array, with unit cell Σ. The antenna resonator is formed between a top metal strip and a bottom metallic plane, that also illustrates the fundamental half wavelength mode. The spacing between two *LC* meta-atoms is given by the antenna length L_A. (b) Room temperature reflectivity spectra of an array of *LC* meta-atoms (blue solid line) and of the same array coupled with antennas with $L_A = 5$ μm (dark green solid lines). The dotted curves are CMT fits. A_1 and A_2 denote the two coupled modes, for which we also provide the electric energy density obtained from finite element method simulations.

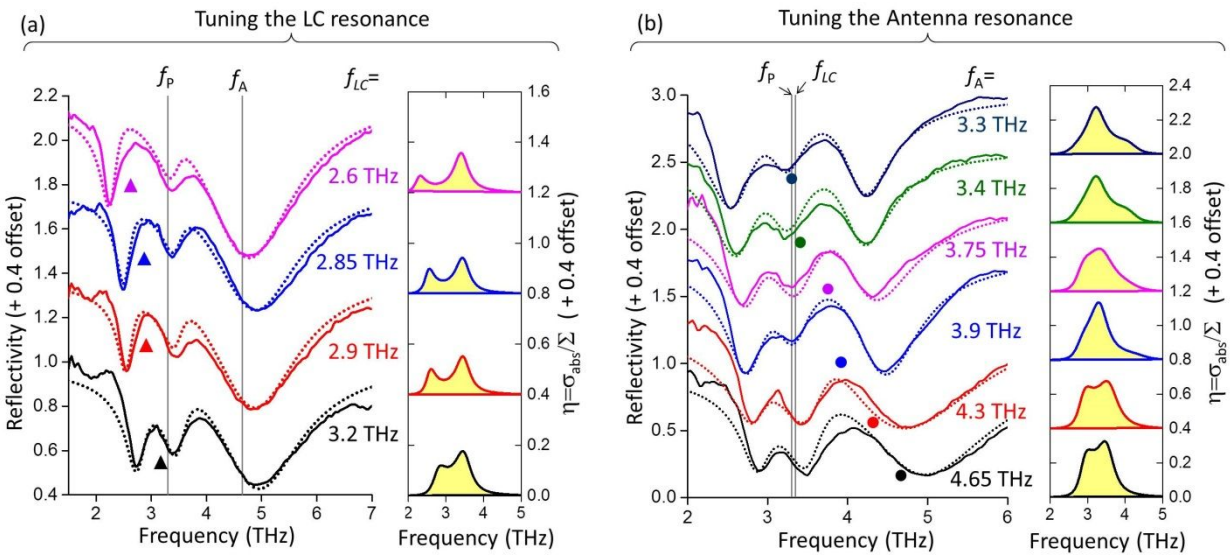

Figure 4. **Fully coupled system** (a) Low temperature (7 K) reflectivity spectra for antenna-coupled LC, for a fixed antenna resonance (f_A = 4.65 THz) and variable LC resonant frequencies. The latter are indicated by numerical values and triangles with respect to the frequency axis. Experimental data is shown in solid lines and CMT fits in dotted lines. Right panel: photon absorption efficiency $\sigma=\eta_{abs}/\Sigma$ from eq.3 for each spectrum. (b) Low temperature (7 K) reflectivity spectra in the case where LC and QW are nearly resonant at $f_{LC}\sim f_P$= 3.3 THz, and the antenna frequency f_A varied. The latter is indicated by numerical values and dots with respect to the frequency axis. Experimental data is shown in solid lines and CMT fits in dotted lines; the corresponding spectra of $\sigma=\eta_{abs}/\Sigma$ are indicated in the right panel.

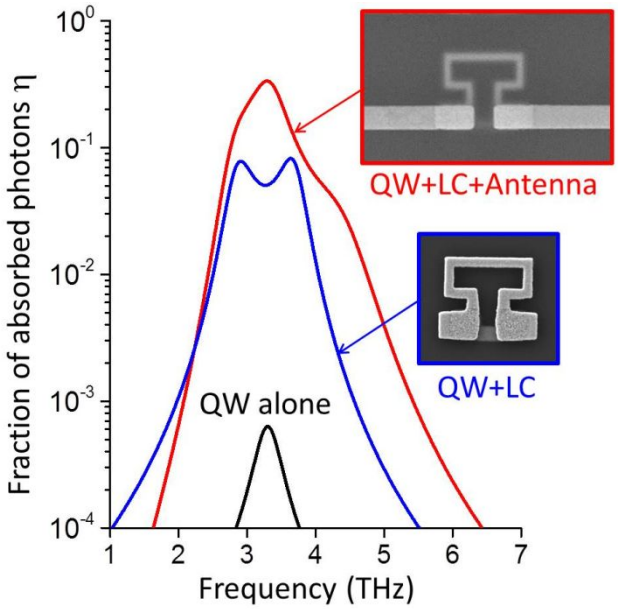

Figure 5. **Absorption engineering from experiments.** Fraction of absorbed photons for the three systems considered in Figure 1. The "QW alone" is modelled as a Lorentzian shape with full width at half maximum $2\gamma_P$=0.4 THz and peak value $\eta_0 = \sigma_{abs}/(3\lambda^2/8\pi\varepsilon) = 6\text{x}10^{-4}$. The "QW+LC" curve corresponds to Figure 2c, and the "QW+LC+Antenna" curve corresponds to the highest values derived from the measurements in Figure 4b (f_A = 3.9 THz).